Intrinsic Compressive Stress in Polycrystalline Films is Localized at Edges of the Grain Boundaries

Enrique Vasco[1] and Celia Polop[2]
[1]Instituto de Ciencia de Materiales de Madrid, CSIC, Sor Juana Inés de la Cruz 3, 28049 Madrid, Spain
[2]Departamento de Física de la Materia Condensada, Instituto Nicolás Cabrera and Condensed Matter Physics Center (IFIMAC), Universidad Autónoma de Madrid, 28049 Madrid, Spain
(Received 25 April 2017; published 22 December 2017)

The intrinsic compression that arises in polycrystalline thin films under high atomic mobility conditions has been attributed to the insertion or trapping of adatoms inside grain boundaries. This compression is a consequence of the stress field resulting from imperfections in the solid and causes the thermomechanical fatigue that is estimated to be responsible for 90% of mechanical failures in current devices. We directly measure the local distribution of residual intrinsic stress in polycrystalline thin films on nanometer scales, using a pioneering method based on atomic force microscopy. Our results demonstrate that, at odds with expectations, compression is not generated inside grain boundaries but at the edges of gaps where the boundaries intercept the surface. We describe a model wherein this compressive stress is caused by Mullins-type surface diffusion towards the boundaries, generating a kinetic surface profile different from the mechanical equilibrium profile by the Laplace-Young equation. Where the curvatures of both profiles differ, an intrinsic stress is generated in the form of Laplace pressure. The Srolovitz-type surface diffusion that results from the stress counters the Mullins-type diffusion and stabilizes the kinetic surface profile, giving rise to a steady compression regime. The proposed mechanism of competition between surface diffusions would explain the flux and time dependency of compressive stress in polycrystalline thin films.

DOI: 10.1103/PhysRevLett.119.256102

Few topics have been so hotly debated by the condensed-matter community as the evolution of intrinsic stress during the formation of polycrystalline thin films and coatings. This subject has deep technological implications, because residual intrinsic stress endures after a polycrystalline film is incorporated into a device. This stress plays a critical role in thermomechanical fatigue [1], which originates from stress regeneration and accumulation under operating conditions. Excessive stress during operation can result in a premature mechanical failure that jeopardizes the reliability of the device and shortens its useful lifespan. To prevent such failures, current devices are given restricted service conditions.

In a polycrystalline thin film growing by the Volmer-Weber mechanism, intrinsic stress evolves in a compressive-tensile-compressive pattern, as indicated by stages I, II, and III in Fig. 1 [2]. During stage I, the nucleated grains are isolated from each other and develop Laplace compression [3]. Stage II occurs when the grains come into contact. During this stage, the cohesive forces between faces come into play, leading to the formation and zipping of grain boundaries (GBs). This process delivers tensile stress [4]. If the adatom mobility is low, further growth develops a porous film under traction. However, under high mobility conditions, the film enters another compressive stage (stage III) during closure and thickening [5–11]. A noteworthy feature of this postcoalescence compression (stage III) is its reversibility [12]: A significant part of the compressive stress relaxes when the flux is interrupted and then recovers once the flux is resumed, as shown in Fig. 1. The fact that the existence of GBs is a prerequisite for reversible postcoalescence compression has been well established [13,14].

The mechanisms responsible for postcoalescence compression have generated intense discussion without a consensus so far. Several mechanisms have been proposed: (A) The Laplace compression that operates during stage I is recovered in stage III after the cohesive forces between coalescing grains decay [5]; (B) adatoms are inserted between surface ledges [6]; (C) adatoms are reversibly inserted into GBs by flux-induced changes in the surface chemical potential [7]; (D) the twisted zipping of GBs between misorientated grains [8]; (E) copious adatom attachment hinders the evolution of GBs towards their equilibrium profiles, resulting in a form of compression by adatom trapping [9]; and (F) flux-induced entropic effects force the reversible insertion of adatoms into GBs under conditions of adatom supersaturation [10]. Those models based on the interaction between grains (A and D) fail to explain the reversibility of the phenomenon, while those based on inserting or trapping adatoms at GBs (C, E, and F) do not fit classical growth theories (e.g., the Zeno effect [15]) that describe the GBs as depleted regions with a lower ratio of adatom density to step density. Despite these and other key points yet to elucidate, the models based on adatom insertion or trapping in GBs currently have wider acceptance.

In our view, the difficulty of reaching a consensus lies in the fact that current models of stress generation, most of them atomistic, attempt to explain the experimental evidence in terms of macroscopic average behaviors, while the microscopic stress distribution is unknown. In this work, we resolve the spatial distribution of the residual intrinsic stress at nanoscale resolution in polycrystalline Au films, using a pioneering method [16] based on atomic force microscopies (AFMs) [force modulation (FMM) [16] and bimodal AFM [17,18]]. These experiments show that the stress is heterogeneously distributed along the grain diameter, being concentrated in narrow strips adjacent and parallel to the GBs (not directed into the GB, as is usually assumed). We interpret this evidence using the Laplace-Young equation, which describes the tension balance at the GB triple junction, within the framework of a competition between different surface diffusions. The results point out that the intrinsic compression in polycrystalline thin films is a consequence of the balance of the surface kinetics vs thermodynamics of these systems.

Figure 1 shows the *in situ* stress evolution during the deposition of a polycrystalline (111)Au film evaporated on (111)Si substrates held at room temperature [19]. The stress-thickness curves are calculated using the Stoney equation [21] from the sample curvatures measured by a homemade multibeam optical stress sensor (MOSS) similar to that proposed by Floro and Chason [22,23]. The thickness-stress curve in Fig. 1 exhibits the typical compression-traction-compression evolution (stages I-II-III) described above. The grains start coalescing after 8 min of deposition

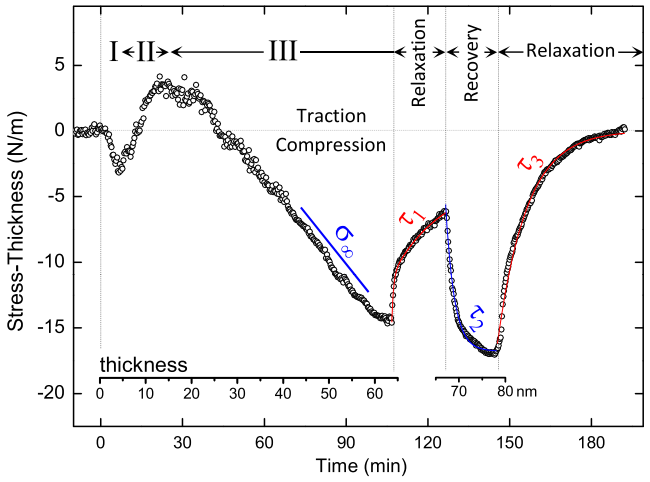

FIG. 1. Stress-thickness curve calculated, by the Stoney equation, from the curvature of polycrystalline (111)Au films. Vertical dashed lines indicate the flux transients: The flux was interrupted for 20 min after 100 min of deposition and then resumed for another 20 min. The symbols correspond to the data, while solid curves denote parametric fits. The fitting parameters are the steady postcoalescence compression ($\sigma_\infty \approx -460$ MPa) and the characteristic times of stress relaxation ($\tau_1 \approx 436$ and $\tau_3 \approx 648$ s) and recovery ($\tau_2 \approx 185$ s). The growth stages (I, II, and III) with different stress behaviors are indicated along the top.

(at this time, the slope of the curve changes from negative to positive, which means that new layers are added under traction) and form a continuous layer at around 30 min. A steady compression ($\sigma_\infty \approx -460$ MPa) is reached after 36 min of growth. This stress relaxes when the flux is interrupted and recovers once the flux is resumed. The first relaxation lasts for 20 min and has a characteristic time $\tau_1 \approx 436$ s. The second relaxation happens at the end of the deposition with $\tau_3 \approx 648$ s. In agreement with previous reports [12], our results reveal that both relaxations progress more slowly than the stress recovery (with $\tau_2 \approx 185$ s) and also that the relaxation times become longer as the film thickness increases ($\tau_3 > \tau_1$).

Figure 2 shows the nanoscale stress mapping of a 600-nm-thick Au film, including (a) AFM topography, (b) FMM amplitude image, (c) stress map, (d) stress histogram, (e) traction-compression map, and (f) stress profiles across a GB. Details on the setups used to map the stress by FMM and bimodal AFM are reported elsewhere [16]. A tessellation filter [24] is included in Figs. 2(a) and 2(e) to illustrate the GB mesh. The topography reveals a granular surface with moderate rms roughness (3.5 nm). The grains have irregular shapes with quasihexagonal symmetry and an average diameter of 150 nm. The FMM amplitude is related to the effective tip-film contact stiffness, and lighter areas on the map correspond to stiffer regions of the film. This apparent stiffening is due to the stress-stiffening effect, as previously described [16]. The stress map in Fig. 2(c) is the result of quantizing this effect. Briefly, the indentation of the film under an AFM-tip load (Hertz model) causes the intrinsic stress to contribute to reinforce or counter the normal pressure generated by this load for stresses of compression or traction, respectively. Thus, the darker (lighter) areas in Fig. 2(c) represent regions under compression (traction).

Figure 2(d) shows the histogram of the stress map in Fig. 2(c). The bins are grouped into five levels: 0 (green) is relaxation; A and A' (red) are low and high compression, respectively; B and B' (blue) are low and high traction, respectively. Note that the residual stress $\langle\sigma\rangle = -0.4$ MPa averaged over the image size ($0.6 \times 0.6\ \mu m^2$) is below the sensitivity of our MOSS [23]. Figure 2(e) shows a map of the discrete stress levels identified. Figure 2(f) displays a characteristic stress profile across the GB [taken along the yellow line in Fig. 2(c)]. Both Figs. 2(e) and 2(f) highlight the heterogeneous spatial distribution of residual intrinsic stress. The stress gradients along the grain diameter are particularly intense. Whereas compression (red areas) often dominates regions $\omega = 25 \pm 7$ nm wide on both sides of the GBs, the inner surfaces of the grains seem to be mostly relaxed (green areas). Between these two regions, annular areas of slight traction [arrowed regions in Fig. 2(f)] frequently appear. Higher tensile stresses (blue areas) occur in the gaps, around where the GBs intercept the surface, and at the surface pinholes. The maps of residual stress

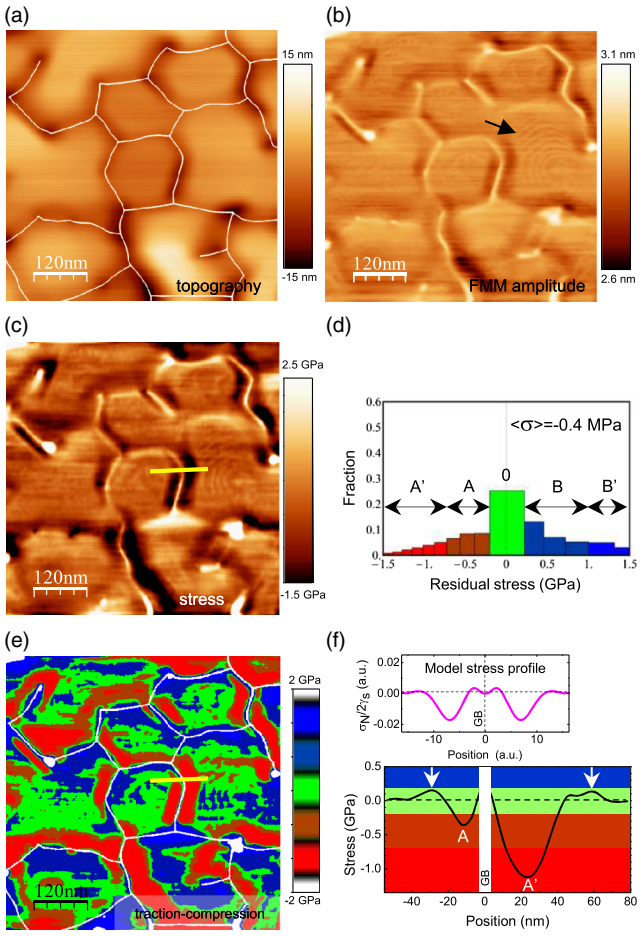

FIG. 2. Characterization of 600-nm-thick polycrystalline (111)Au films by FMM. (a) AFM topography, (b) FMM amplitude image, (c) stress map, (d) stress histogram, (e) traction-compression map, and (f) model and experimental stress profiles along the yellow line in (c) and (e). The model profile in (f) is the same as that computed in Fig. 3(c) (see details below). The colors in (d)–(f) correspond to five stress levels: relaxation (0, green), low and high compression (A, red, and A', light red), and low and high traction (B, blue, and B', light blue). The widths of the histogram bins (d) are taken from the uncertainty in the stress determination due to the FMM indentation resolution (≈0.2 Å [16]). The arrows in (b) point to vicinal structures on grain tops, while those in (f, bottom) indicate slightly tensile regions. A grain tessellation filter illustrates the GB mesh in (a) and (e) [24]. Other white features in (e) are surface pinholes.

obtained by bimodal AFM [19] are similar to those imaged by FMM, which supports our results.

Equilibrium profiles.—The equilibrium profile of the surface $h(\vec{r})$ of a polycrystalline solid, around a GB at $r = 0$, follows the dependency [25,26]:

$$h_e(r) = \eta h_{\mathrm{GB}} \mathrm{ierfc}(m_0 r/\eta h_{\mathrm{GB}}), \tag{1}$$

where h_{GB} is the GB triple-junction depth ("gap depth" hereafter); $\mathrm{ierfc}(x)$ is the integral of the complementary error function; $m_0 = \partial_r h_e|_{r=0}$ is the equilibrium slope at the GB triple junction; and $\eta = 1.77$. m_0 results from the balance between tensions [inset in Fig. 3(a)] $\gamma = 2\gamma_s \sin[\arctan(m)] - \gamma_{\mathrm{gb}}$, where γ_s and γ_{gb} are the surface and GB energies per unit area, respectively, and $\arctan(m)$ denotes the wetting angle. This balance induces an intrinsic stress whose component normal to the surface is given by the Laplace-Young equation: $\sigma_N = -\vec{\nabla}_s \gamma$, such that the mechanical equilibrium $\sigma_N = 0$ implies $m_0 = \tan\{\arcsin[\gamma_{\mathrm{gb}}/2\gamma_s]\}$. On the rough surface far from the GB, the surface tension governs the tension balance $\gamma = \gamma_s$, and consequently $\sigma_N \approx 2\gamma_s \kappa(\vec{r})$, where $\kappa(\vec{r}) \approx -\nabla^2 h(\vec{r})$ is the local surface curvature. The equilibrium condition implies $\kappa(\vec{r}) = 0$ and $\partial_r h_e|_{r\to\infty} = \mathrm{const} = 0$, which means that the equilibrium profile far from a GB is defined along a flat surface. The equilibrium profiles $h_e(r)$ according to Eq. (1) are plotted in Fig. 3 (red curves).

Short-term diffusive profiles.—According to the Mullins [26] and Srolovitz [31] theories, surface diffusion makes the surface evolve towards a characteristic profile obeying the relation

$$(1/\Omega)\cdot \partial_t h = -\phi \nabla^4 h(r,t) - \phi N \gamma_s^{-1} \nabla^2 [\sigma_N^2(r,t)/2M], \tag{2}$$

where Ω is the atomic volume and $\phi = D_s \gamma_s \Omega n_\infty / k_B T$ is the drift velocity of the adatoms with D_s and $n_\infty = n(r \to \infty)$ denoting the surface diffusion coefficient and the equilibrium adatom density far from the GB, respectively, while $k_B T$ preserves its usual meaning. The second term in Eq. (2) (that considering the Srolovitz-type surface diffusion) is described below. The Mullins-type surface diffusion (first term) is characterized by a current of adatoms $\vec{J} = -\phi \vec{\nabla}_s \kappa$ driven by gradients of the surface curvature κ, which provides an estimate of the local density of dangling bonds.

Figure 3 shows the evolution of surface profiles around a GB gap [Fig. 3(a)] and a hollow [Fig. 3(b)]. The latter case represents a local feature of the rough surface far from a GB. The profiles are calculated at several stages during filling, which is supplied by the surface diffusion of adatoms from a flux. The profiles are computed by numerical integration of Eq. (2) assuming the boundary conditions in Ref. [27]. Note that, unlike the GB, the surface slope inside the hollow is unconstrained. Both features are given similar initial profiles $h(r,0)$ [black curves in Figs. 3(a) and 3(b), which are similar to the normalized equilibrium profile in the vicinity of a GB with $m_0 = 0.3$], in order to highlight the differences between their evolutions and with the corresponding equilibrium profiles $h_e(r)$ (red curves) for the same deposited volume. The longest-time profiles (green curves) provide a good estimate of the time-saturated diffusive profiles [i.e., $h_d(r) = h(r, 10^4)$ when the two terms in Eq. (2) cancel each other].

The following conclusions can be drawn from a comparison of Figs. 3(a) and 3(b): (a) The hollow disappears by surface diffusion [Fig. 3(b)], but the GB gap does not

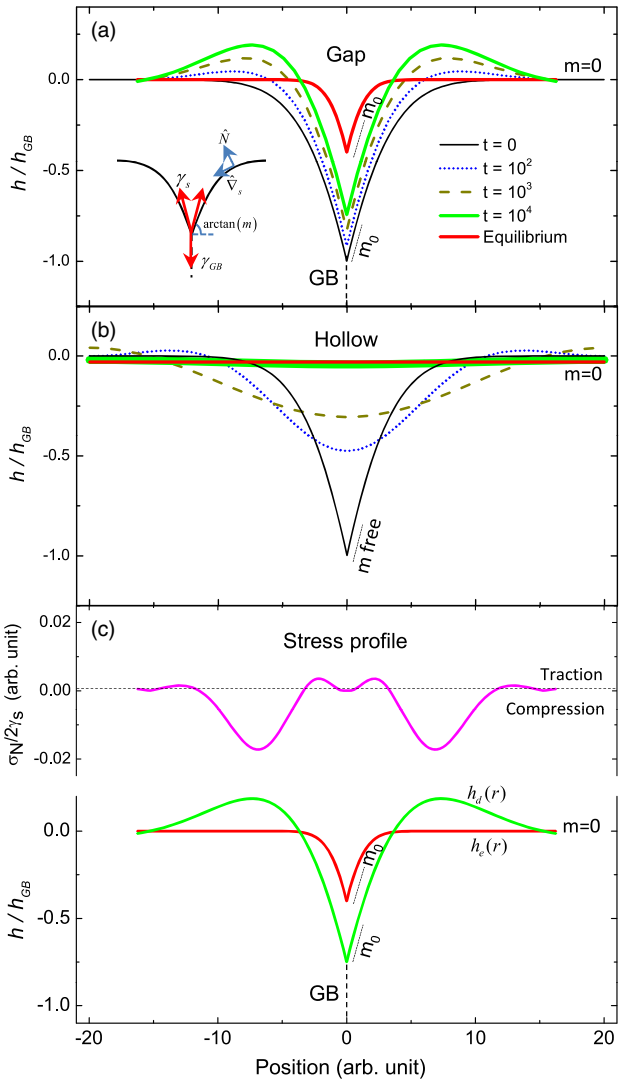

FIG. 3. Evolution of the normalized surface profiles for a GB gap (a) and a hollow (b) by integration of Eq. (2). The slope boundary conditions [27] and the initial profiles $h(r,0)$ (black curves) are depicted. The equilibrium profiles (red curves) are derived from Eq. (1), not from diffusion. The integration is carried out in arbitrary units of length and time for $\phi = 1$. The profiles are scalable to physical magnitudes by the change of variables $h(r,t) = h(S_r r, S_t t)$, with the scaling factors $S_r = 1$ nm/unit and $S_t = S_r^4/\phi\Omega \sim 10$ ms/unit [28]. The inset in (a) diagrams the tension balance at the GB triple junction. Panel (c) shows a stress profile (upper plot) across a GB gap. This profile is calculated from Eq. (3), using the surface diffusive profile $h_d(r) = h(r, 10^4)$ and the equilibrium profile $h_e(r)$ (both are repeated below for convenience).

[Fig. 3(a)]. Even if the GB gap were mostly filled, the equilibrium slope would persist at the boundary, resulting in a differential gap. Completely erasing a GB requires a recrystallization process involving GB motion and/or grain reorientation, such that $\gamma_{\rm gb} \to 0$. (b) The fact that the slope at the GB triple junction is constrained to a different value than the slope associated with the surface far from the GB implies that profiles originated by surface diffusion always differ from those determined by equilibrium [compare green and red curves in Fig. 3(a)]. (c) This difference reveals itself mainly at the edges of the gap, where the diffusing adatoms accumulate, forming sharp ridges [26]. This accumulation happens because the slope constraint hinders relaxation of the curvature gradient $\vec{\nabla}_s\kappa$ close to the GB triple junction. From an atomistic viewpoint, the accumulation can be understood as due to changes in the surface current of adatoms along the gap-side profile, such that $\vec{\nabla}\vec{J} \neq 0$. Thus, while the diffusion driving force $\vec{\nabla}_s\kappa$ towards the undercoordinated GB is preserved, the effective diffusion coefficient D_s decreases within the gap where, according to the Zeno effect [15], there is a higher density of step-edge barriers to cross. This behavior is quite different from that occurring in the hollow [Fig. 3(b)], where surface diffusion relaxes the curvature gradient quickly without any meaningful accumulation of adatoms.

Stress profiles.—Where the curvature κ_d of the diffusive profile differs from the curvature κ_e of the equilibrium profile, a stress is generated in the form of Laplace pressure:

$$\sigma_N(r,t) \approx 2\gamma_s[\kappa_e(r,t) - \kappa_d(r,t)]. \tag{3}$$

This pressure attempts to mechanically reduce the changes in surface curvature that result from the adatom accumulation. Figure 3(c) shows the normalized stress profile (upper plot) caused by this accumulation at the edges of a GB gap. The stress oscillates from traction inside the gap to compression at the edges, then returns to slight traction as the adatom density approaches its equilibrium value, and finally relaxes far from the GBs. This profile [labeled "model profile" in Fig. 2(f)] exhibits excellent qualitative agreement with the experimental stress profiles [Fig. 2(f)] for the region reachable by the AFM tip [24]. A rigorous discussion of this comparison is presented in Ref. [19]. The compressive regions in the stress profile, where $|\kappa_d| > |\kappa_e|$, provide the predominant contribution, this being responsible for the postcoalescence compression under deposition and operating conditions where the surface mobility is enhanced.

Long-term diffusive profiles.—As discussed above, the formation of ridges at the gap edges increases the Laplace compression σ_N. This compression generates a Srolovitz-type surface diffusion [31], second term in Eq. (2), which counters the Mullins-type surface diffusion and stabilizes the diffusive profiles. In the Srolovitz-type diffusion, the current of adatoms $\vec{J} = -\phi N\gamma_s^{-1}\vec{\nabla}E_e$ is induced by the gradient of the accumulated strain energy per unit volume $E_e = \sigma_N^2/2M$, where M is the biaxial modulus of the film and $N = n_{\rm ridge}/n_\infty$ estimates the excess of adatoms condensed in the ridges. When the two terms in Eq. (2) cancel each other, the surface profile becomes steady, $\partial_t h \approx 0 \Rightarrow h_{\rm GB} \to$ const, which implies, according to Eq. (3), that σ_N approaches the constant value $\sigma_N \to \sigma_\infty$ observed during stage III. This result agrees with the

prediction of Chason [12], suggesting that the steady compression is reached when the rate of GB formation coincides with the deposition rate, which is equivalent to saying that the gap depth becomes constant. Similarly, other distinctive features of the intrinsic stress (reversibility with the flux, kinetics of relaxation and recovery [12], and the relative insensitivity of such a kinetics to *in situ* variations of the flux and temperature [14,32]) would result from the proposed mechanism of competition between surface diffusions, as we shall demonstrate in forthcoming work.

Two conclusions can be drawn from our results: First at all, the present study demonstrates that nanoscale stress mapping based on AFM techniques (here FMM and bimodal AFM) has great potential to disclose the nature of the intrinsic stress in solids. Second, we used stress mapping to reveal the key role played by surface diffusion around grain boundaries in the generation of intrinsic compression in polycrystalline thin films. We explain these findings comprehensibly in light of the Mullins and Srolovitz theories for surface diffusion of adatoms, driven by surface curvature and strain-energy gradients, respectively. Mullins-type diffusion towards the GBs generates a kinetic surface profile characterized by adatom accumulation at the edges of the GB gap. This kinetic profile is different from the mechanical equilibrium profile predicted by the Laplace-Young equation. Where the curvatures of both profiles differ, a Laplace compression is generated. This compression at the gap edges (not inside the GBs, as previously supposed) is the major contribution to the intrinsic stress during the postcoalescence regime. The Srolovitz-type diffusion resulting from the stress counters the Mullins-type diffusion and stabilizes the intrinsic stress to a constant compression under high atomic mobility conditions.

The authors thank Alma P. Perrino and Ricardo García for the bimodal AFM measurements and fruitful discussions on nanoscale stress mapping. This work was supported by the Spanish Ministerio de Economía y Competitividad under Project No. MAT2014-52477-C5-5-P.

[1] *Elements of Metallurgy and Engineering Alloys*, edited by F. C. Campbell (ASM International, Materials Park, 2008), Chap. 14.
[2] J. A. Floro, S. J. Hearne, J. A. Hunter, P. Kotula, E. Chason, S. C. Seel, and C. V. Thompson, J. Appl. Phys. **89**, 4886 (2001).
[3] S. P. A. Gill, H. J. Gao, V. Ramaswamy, and W. D. Nix, J. Appl. Mech. **69**, 425 (2002).
[4] W. D. Nix and B. M. Clemens, J. Mater. Res. **14**, 3467 (1999).
[5] R. Koch, D. Hu, and A. K. Das, Phys. Rev. Lett. **94**, 146101 (2005).
[6] F. Spaepen, Acta Mater. **48**, 31 (2000).
[7] E. Chason, B. W. Sheldon, L. B. Freund, J. A. Floro, and S. J. Hearne, Phys. Rev. Lett. **88**, 156103 (2002).
[8] A. González-González, C. Polop, and E. Vasco, Phys. Rev. Lett. **110**, 056101 (2013).
[9] H. Z. Yu and C. V. Thompson, Appl. Phys. Lett. **104**, 141913 (2014).
[10] A. Saedi and M. Rost, Nat. Commun. **7**, 10733 (2016).
[11] B. Fu, W. An, C. Turner, and G. Thompson, Phys. Rev. Lett. **105**, 096101 (2010).
[12] E. Chason, Thin Solid Films **526**, 1 (2012).
[13] D. Magnfält, A. Fillon, R. D. Boyd, U. Helmersson, K. Sarakinos, and G. Abadias, J. Appl. Phys. **119**, 055305 (2016).
[14] D. Flötotto, Z. M. Wang, L. P. H. Jeurgens, and E. J. Mittemeijer, J. Appl. Phys. **118**, 055305 (2015).
[15] T. Michely and J. Krug, *Islands, Mounds and Atoms* (Springer, New York, 2004), Chaps. 3 and 4.
[16] C. Polop, E. Vasco, A. P. Perrino, and R. Garcia, Nanoscale **9**, 13938 (2017).
[17] R. Garcia and R. Proksch, Eur. Polym. J. **49**, 1897 (2013).
[18] E. T. Herruzo, A. P. Perrino, and R. Garcia, Nat. Commun. **5**, 3126 (2014).
[19] See Supplemental Material at http://link.aps.org/supplemental/10.1103/PhysRevLett.119.256102 for details concerning thermal and residual stresses, and stress mapping by bimodal AFM, which includes Ref. [20].
[20] F. C. Nix and D. MacNair, Phys. Rev. **60**, 597 (1941).
[21] G. G. Stoney, Proc. R. Soc. A **82**, 172 (1909).
[22] J. A. Floro and E. Chason, Appl. Phys. Lett. **69**, 3830 (1996).
[23] The MOSS was implemented on an antivibration platform incorporating a laser-position stabilization system to prevent spherical aberrations. This setup allows us to determinate sample curvatures up to $\kappa \sim 1/40$ km^{-1} from relative displacements of the beams as small as $\delta d = \pm 0.05$ pixel, measured by a high-resolution CCD camera. The stress sensitivity of our MOSS is $\delta\sigma = (\delta d/d)[M_{\mathrm{Si}} h_{\mathrm{Si}}^2 \cos(\theta)/12 L h_{\mathrm{Au\,film}}] \approx 2$ MPa, according to the Stoney equation, for relative displacements averaged over 8–10 spots (spaced at $d = 160$-180 pixels) with $h_{\mathrm{Au\,film}} = 600$ nm, $h_{\mathrm{Si}} = 350$ μm, $M_{\mathrm{Si}} = 230$ GPa, $L = 40$ cm, and $\theta = 45°$.
[24] The line thickness of the tessellation filter (~5.5 nm, diameter of the tip-sample contact [16]) provides an estimate of which areas are inaccessible to the AFM tip.
[25] H. S. Carslaw and J. C. Jeager, *Conduction of Heat in Solids* (Oxford University, New York, 1947).
[26] W. W. Mullins, J. Appl. Phys. **28**, 333 (1957).
[27] Boundary conditions for Eq. (2): $\nabla h(\pm r_{\mathrm{GB}}, t) = \pm m_0$ (slope constraint at the GB triple junction), $\nabla h(+\infty, t) = \nabla h(-\infty, t) \equiv 0$, and $h(+\infty, t) = h(-\infty, t) \equiv 0$ (equilibrium slope and fixed periodic conditions far from the GB, respectively).
[28] The time-scaling factor S_t was estimated by considering a diffusion length of $\lambda_d = 10^2$ nm (~grain size), which implies $n_\infty = \lambda_d^2 F/4\Omega D_s \approx 1.8 \times 10^{-5}$ nm^{-2} for a deposition rate of $F = 0.6$ nm/min; $D_s = 8.5 \times 10^{-9} \exp(-0.12/k_B T)\mathrm{m}^2/\mathrm{s}$ [29]; $\Omega = 1.6 \times 10^{-29}$ m^3/atom; and $\gamma_s = 1.175$ J/m^2 [30].
[29] P. M. Agrawal, B. M. Rice, and D. L. Thompson, Surf. Sci. **515**, 21 (2002).
[30] C. W. Mays, J. S. Vermaak, and D. Kuhlmann-Wilsdorf, Surf. Sci. **12**, 134 (1968).
[31] D. J. Srolovitz, Acta Metall. **37**, 621 (1989).
[32] J. Leib and C. V. Thompson, Phys. Rev. B **82**, 121402(R) (2010).